Neuromechanical Control for Hexapedal Robot Walking on Challenging Surfaces and Surface Classification

Xiaofeng Xiong[1], Florentin Wörgötter[1] and Poramate Manoonpong[2,1]

[1]*Bernstein Center for Computational Neuroscience (BCCN), The Third Institute of Physics, Georg-August-Universität Göttingen,D-37077 Göttingen, Germany.*

[2]*Center for Biorobotics, Mærsk Mc-Kinney Møller Institute, University of Southern Denmark, 5230 Odense M, Denmark.*

Abstract

The neuromechanical control principles of animal locomotion provide good insights for the development of bio-inspired legged robots for walking on challenging surfaces. Based on such principles, we developed a neuromechanical controller consisting of a modular neural network (MNN) and of virtual agonist-antagonist muscle mechanisms (VAAMs). The controller allows for variable compliant leg motions of a hexapod robot, thereby leading to energy-efficient walking on different surfaces. Without any passive mechanisms or torque and position feedback at each joint, the variable compliant leg motions are achieved by only changing the stiffness parameters of the VAAMs. In addition, six surfaces can be also classified by observing the motor signals generated by the controller. The performance of the controller is tested on a physical hexapod robot. Experimental results show that it can effectively walk on six different surfaces with the specific resistances between 9.1 and 25.0, and also classify them with high accuracy.

Keywords:
Agonist and antagonist muscle model, legged locomotion, biological inspired locomotion, hexapod robot.

1. Introduction

Neuromechanical models for animal locomotion combine neural circuits (e.g., central pattern generators, CPGs) and biomechanics (e.g., muscles). They are also used to study the interplay of muscles, CPGs, and sense organs [1], which provides good insights into developing bio-inspired locomotion systems [2]. Employing such models leads to adaptation and energy efficiency of locomotion of the bio-inspired systems [3, 4, 5].

The energy efficiency of bio-inspired walking systems is typically measured by specific resistance [6, 7]. Lower specific resistance corresponds to more efficient walking. Neuromechanical controllers exploit muscle-like mechanisms as well as neural mechanisms for effective legged robot control. In contrast, isolating them results in energy inefficient locomotion [8], thereby leading to high specific resistances [9].

For instance, the specific resistance of a hexapod robot (i.e., Gregor I) during walking over an uneven surface (i.e., obstacle course) is 70 when only a cellular neural network is used as its CPG [10]. Combining CPGs with forward models can improve the energy efficiency of a hexapod robot. For example, a CPG combined with an adaptive forward model enables a hexapod robot (i.e., AMOS) to walk over an uneven surface (i.e., fine gravel) with the specific resistance of 55.5 [11]. Adaptive leg motions generated by the neural controllers of Gregor I and AMOS depend only on the changes of neural activities of the controllers for walking over uneven surfaces. However, owing to energy efficiency [12], there are no changes detected in neural activities for controlling key muscles or performing precise limb coordination of cockroaches when walking over an uneven surface (i.e., obstacles up to three times cockroach hip height) [13]. This finding shows that cockroaches perform adaptive leg motions and compensate perturbations by relying more on their biomechanics (e.g., muscles), thereby leading to energy efficiency.

Muscles also play a vital role in legged locomotion over different terrains [14, 15, 16, 17]. In robotic applications, muscle-like mechanisms (e.g., Shape Memory Alloy (SMA) actuators) can be used for controlling lightweight legged robots. However, such SMA actuators are energy inefficient owing to their slow cycle speed. For example, the specific resistance of a small legged robot is over 12,000 when its joints are mainly actuated by SMA actuators [18]. In contrast, our virtual agonist-antagonist mechanisms (VAAMs, i.e., muscle-like mechanisms) proposed here lead to smaller specific resistances of a hexapod robot during walking on different surfaces (described below). The VAAMs can also generate variable compliant leg motions which rely only on force sensing at the end effectors of the robot legs. This technique is different from two classical methods (i.e., active and passive compliance). Typically, active compliance [19] requires the components of force/torque sensing at each joint while passive compliance [20] depends heavily on physical passive components, e.g., passive springs or artificial muscles. These components make legged robots heavier and mechanically more complex, therefore making it difficult to implement on small legged robots (weight less than 8 kg) [21].

Combining the VAAMs with a modular neural network (MNN) results in a neuromechanical controller which is able

to control, e.g., a small hexapod robot (5.4 kg). In principle, the MNN is for generating basic coordinated movements while the VAAMs are for energy efficient walking and variable compliant leg motions. Without any passive mechanisms or torque and position feedback at each joint, the variable compliant leg motions are achieved by only changing the damper or stiffness parameters of the VAAMs [22]. Proper setups of the stiffness parameters allow a physical hexapod robot to effectively walk on different surfaces, i.e., fine gravel, coarse gravel, very coarse gravel, floor, snow and sponge surfaces.

In addition, adaptive compliance motion will also help legged robots to classify surfaces. Generally, surface classification has been implemented on legged robots based on multiple sensing (e.g., current and angular positions) [23, 24], force/torque sensing [25, 26], vibration sensing [27, 28] and visual perception [29, 30]. Visual perception using conventional technique [31] cannot work well in classifying the surfaces of non-distinguishable features (e.g, snow). Owing to natural vibrations of legged robots, vibration sensing may not perform well for classifying surfaces either [32]. Compared to multiple sensing, force sensing can still provide precise surface classifications by using a simple algorithm. Force sensing embedded in the VAAMs allows a physical hexapod robot to well classify six different surfaces with high accuracy (i.e., $\geq 89\%$).

2. Neuromechanical controller of a hexapod robot

Here we use the hexapod robot AMOS (5.4 kg weight, see Fig. 1) as our experimental platform. It has six three-jointed legs. Each three-jointed leg has a TC (Thoraco Coxal) joint allowing forward and backward motions, a CTr (Coxa Trochanteral) joint allowing elevation and depression motions, and a FTi (Femur Tibia) joint allowing extension and flexion motions (see Fig. 1 (b)). Each joint is physically driven by a standard servo motor (i.e., HSR-5990TG). There is a force sensor (i.e., FS Series Force Sensor) used for detecting an analog force signal at each leg (see fc_{1-6} in Fig. 1 (a)). A current sensor installed inside the body of the hexapod robot is used to measure the electrical current supplied to all motors of the robot. Here, the current sensor signal is used to calculate power consumption during walking. The sensory data are transmitted via an RS232 serial connection to an external PC on which a controller is implemented. Here a neuromechanical controller (see Fig. 2) is employed to generate the adaptive and energy efficient walking behavior of the robot. The controller consists of a modular neural network (MNN) and virtual agonist-antagonist mechanisms (VAAMs). The final motor commands of the controller are sent to the robot via the serial connection.

2.1. Modular Neural Network (MNN)

The modular neural network (MNN) is a biologically-inspired hierarchical neural controller [33]. The MNN generates signals for inter- and intra-leg coordination of the hexapod robot. The MNN consists of a central pattern generator (CPG, see Fig. 3 (a)), a phase switch module (PSM, see Fig. 3 (b)) and two velocity regulating modules (VRMs, see Fig. 3 (c)). All
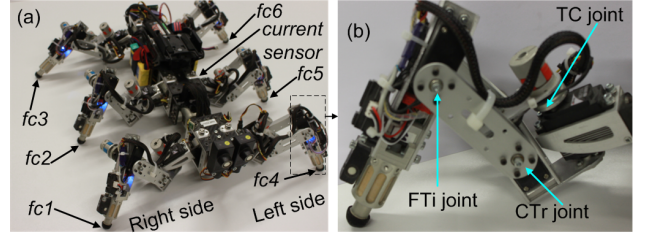

Figure 1: The hexapod robot AMOS. (a) The hexapod robot and its sensors. $fc_{(1-6)}$ are force sensors. (b) Leg with three degrees of freedom.
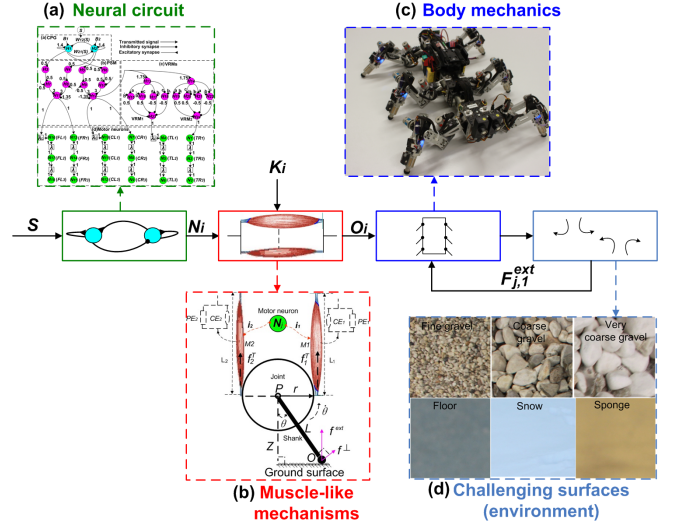

Figure 2: Neuromechanical control for the hexapod robot. Via neural outputs N_i ($i = 1, 2, \ldots, 17, 18$), a neural circuit activates muscles that generate position commands (i.e., O_i) to move the joints of AMOS legs. The legs then interact with the environment, which produces force feedback (i.e., $F_{j,1}^{ext}$, $j = 1, 2, \ldots, 5, 6$) back to the system. (a) Neural circuit. It is the modular neural network (MNN) (see Fig.3) where $S \in [0.01, 0.18]$ is the modulatory input determining the speed of robot legs. The speed of its leg motion increases with increasing S. (b) Muscle-like mechanisms which are here virtual agonist-antagonist mechanisms (VAAMs) (see Fig.5). (c) Body mechanics of AMOS. (d) Challenging surfaces (environment) which are here fine gravel, coarse gravel, very coarse gravel, slippery floor, snow, and elastic sponge.

neurons of the MNN are modeled as discrete-time, non-spiking neurons. The activation H_i of each neuron develops according to:

$$H_i(t) = \sum_{j=1}^{m} W_{ij} \, o_j(t-1) + B_i, \quad i = 1, \ldots, m, \quad (1)$$

where m denotes the number of units, B_i is an internal bias term (i.e., stationary input) to neuron i, W_{ij} is the synaptic strength of the connection from neuron j to neuron i. The output o_i of all neurons of the MNN is calculated using the hyperbolic tangent (tanh) transfer function, i.e., $o_i = \tanh(H_i), \in [-1, 1]$. The weights W_{ij} are manually designed, except weights a, b, and c which are obtained by backpropagation learning (see Fig.3 (c)). For more details of determining the weights W_{ij}, we refer to our previous work [34].

The CPG consists of only two neurons with full connectivity (see Fig. 3(a)), where B_1 and B_2 are set to 0.01. The weights

W_{12} and W_{21} are given by:

$$W_{12}(S) = 0.18 + S, W_{21}(S) = -0.18 - S, \qquad (2)$$

where $S \in [0.01, 0.18]$ is the input of the MNN, which determines different walking patterns of the robot. The speed of its leg motion increases with increasing S. Here, we set S to 0.04 resulting in slow walking behavior, which leads to stable and energy-efficient locomotion on uneven surfaces [11].

The PSM is a generic feed-forward network consisting of three hierarchical layers with ten hidden neurons (i.e., H_3-H_{12}) (see Fig. 3 (b)). The outputs of the PSM are projected to the FTi (i.e., $F(R, L)_{(1,2,3)}$) and CTr (i.e., $C(R, L)_{(1,2,3)}$) motor neurons (see Fig. 3 (d)), as well as to the neurons H_{13} and H_{14} of the two VRMs (see Fig. 3 (c)). The VRMs are feed-forward networks projecting their outputs to the TC motor neurons $T(R, L)_{(1,2,3)}$ (see Fig. 3 (d)).

In the neuromechanical controller, the outputs N_{1-18} of the motor neurons are the neural activities of the joints of the hexapod robot. N_{1-18} enable the legs to perform fast swing and slow stance phases (see Fig.4). Delays λ_L and λ between the motor neurons are fixed (see Fig. 3 (d)). For more details of the MNN, we refer to our previous work [11].

In our previous work [11], adaptive leg motion depends on changing of the outputs of the MNN which are controlled by additional forward models. In contrast, the proposed neuromechanical controller here only relies on changing the parameters of the muscle-like mechanisms as in cockroach locomotion [13]. Changing the mechanical parameters of the muscle-like mechanisms (i.e., virtual agonist-antagonist mechanism (VAAM)) allows the hexapod robot to not only perform adaptive locomotion, but also achieve more energy-efficient locomotion.

2.2. Virtual Agonist-antagonist Mechanism (VAAM)

The virtual agonist-antagonist mechanism (VAAM) consists of a pair of agonist and antagonist mechanisms (see Fig. 5(a)). It produces active and passive forces using its contractile and parallel elements (CEs and PEs, see Fig. 5(b)). In Fig. 5(a), a physical joint is driven by a pair of the VAAM (i.e., $M1$ and $M2$). Virtual means that the joint, physically driven by a standard servo motor, imitates muscle-like behaviors as if it were driven by a pair of physical agonist and antagonist muscles. The joint actuation relies on the CEs, while the PEs govern joint compliance.

The parallel elements (i.e., PEs) are modeled as spring-damper systems (see Fig. 5(b)) in term of Voigt muscle model [35]. The matrix $[f_1^P, f_2^P]^T$ of passive forces created by $PE_{(1,2)}$ is the sum of two Hadamard products:

$$[f_1^P, f_2^P]^T = \Gamma_{2\times1} \circ L_{2\times1} + \Phi_{2\times1} \circ V_{2\times1}, \qquad (3)$$

where

- $\Gamma_{2\times1}$ is the matrix of stiffness coefficients of $PE_{(1,2)}$, i.e., $\Gamma_{2\times1} = [K, K]^T$;

- $L_{2\times1}$ is the matrix of displacements of $PE_{(1,2)}$, i.e., $L_{2\times1} = [l_1^P - l_0, l_2^P - l_0]^T$. l_0 is the initial length of $PE_{(1,2)}$;
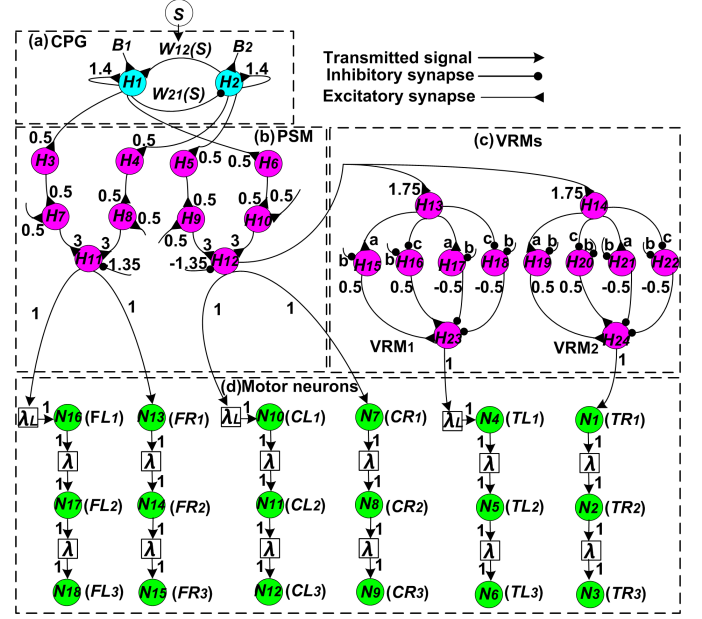

Figure 3: Modular neural network. There are three different neuron groups: input neuron (S), hidden neurons (H_{1-24}) and output neurons (N_{1-18}). The input neuron is used to control walking patterns of the hexapod robot. The hidden neurons are divided into three modules: CPG, PSM and VRMs, which have different functionalities (see text for details). The output neurons represent the neural activities of the joints of the robot. All connection strengths together with bias terms are indicated by the small numbers except some parameters of the VRMs ($a = 1.7246, b = -2.48285, c = -1.7246$). Delays λ_L and λ between output neurons are set to 48 time steps and 16 time steps, respectively. The abbreviations are: $TR(L)_{1,2,3}$ = TC joints of the Right(Left) Front, Middle, Hind legs, $CR(L)_{1,2,3}$ = CTr joints of the Right(Left) Front, Middle, Hind legs, $FR(L)_{1,2,3}$ = FTi joints of the Right(Left) Front, Middle, Hind legs.
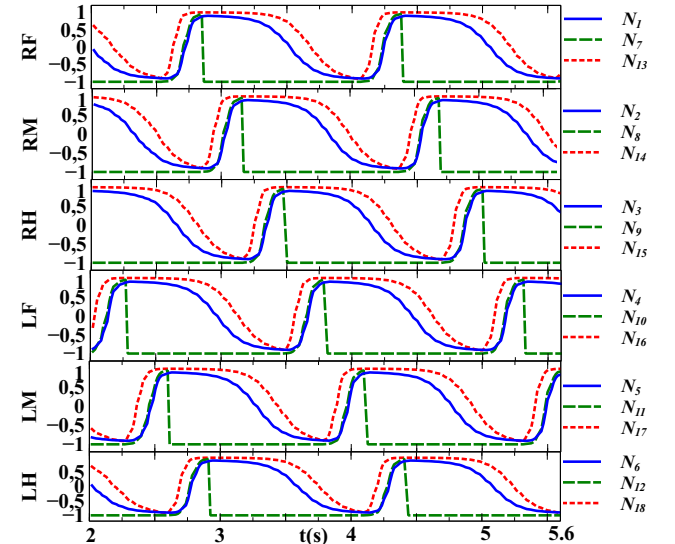

Figure 4: Outputs of the motor neurons N_{1-18}. Here the input S of the modular neural network is set to 0.04. This results in slow walking behavior with a wave gait. Abbreviations are: R(F, M, H) = Right (Front, Middle, Hind) leg, L(F, M, H) = Left (Front, Middle, Hind) leg.

- $\Phi_{2\times1}$ is the matrix of damper coefficients of $PE_{(1,2)}$, i.e., $\Phi_{2\times1} = [D, D]^T$;
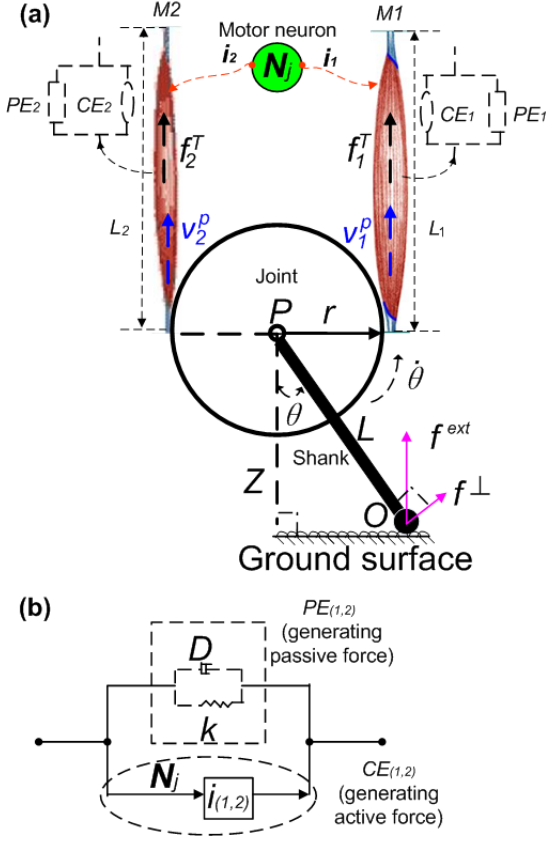
Figure 5: Virtual agonist-antagonist mechanism (VAAM) for joint control interacting with the ground surface. (a) The physical joint P is driven by a pair of the VAAM (i.e., $M1$ and $M2$) with the lengths L_1 and L_2. The interaction results in an external force f^{ext}, which drives the joint P with the radius r via the shank with the length L. f^{ext} is sensed by a force sensor (i.e., O), and $f^{\perp}$ is the amount of f^{ext} directly perpendicular to the position of the joint P. θ is the rotational angle of the joint P relative to the absolute frame Z. (b) The agonist and antagonist mechanisms consist of contractile and parallel elements ($CE_{(1,2)}$ and $PE_{(1,2)}$). $PE_{(1,2)}$ are spring-damper systems producing passive forces. $CE_{(1,2)}$ generate active forces depending on the neural activity N_j and the activity strengths $i_{(1,2)}$ (i.e., $i_{(1,2)} \in [-1, 1]$). The neural activity N_j is one of the outputs N_{1-18} of the modular neural network (see Fig.3 (d)).

- $V_{2\times 1}$ is the matrix of velocities of $PE_{(1,2)}$, i.e., $V_{2\times 1} = [v_1^P, v_2^P]^T$ (see v_1^P and v_2^P in Fig. 5(a)).

The active forces produced by the CEs are approximated by the product of the neural activity N_j and the activity strengths $i_{(1,2)}$. The matrix $[f_1^C, f_2^C]^T$ of the active forces generated by $CE_{(1,2)}$ (see Fig. 5 (b)) is represented by:

$$[f_1^C, f_2^C]^T = N_j \times [i_1, i_2]^T, \qquad (4)$$

where

- N_j is the neural activity of $CE_{(1,2)}$ (i.e., $N_j \in [-1, 1]$). It is one of the outputs N_{1-18} of the MNN (see Fig. 3 (d));

- $[i_1, i_2]^T$ is the matrix of activity strengths for $CE_{(1,2)}$ (i.e., $i_{(1,2)} \in [-1, 1]$).

The total forces f_1^T and f_2^T are the sum of the active and passive forces produced by the muscle pair ($M1$ and $M2$). The

antagonist mechanism $M2$ (see Fig. 5 (a)) resists the extension of the joint angle θ when receiving an external force f^{ext}, which is sensed by a force sensor. Simultaneously, the agonist mechanism $M1$ (see Fig. 5 (a)) produces an opposing force against $M2$. Therefore, the directions of f_1^T and f^{ext} are counter-clockwise when the direction of f_2^T is clockwise. For more details of the VAAM, we refer to our previous work [9].

We apply Euler's law to the rotation of the joint P (see Fig. 5(a)). The net torque $\sum \tau$ acting on the joint P is equal to the product of its moment of inertia I and angular acceleration $\ddot{\theta}$. It is given by:

$$I\ddot{\theta} = \sum \tau = \tau(f^{ext}) + \tau(f_1^T) + \tau(f_2^T). \qquad (5)$$

Derived from Eq.(5), the motion equation of the joint P is given by:

$$I\ddot{\theta} = \underbrace{f^{ext} \sin(\theta)L}_{\text{torque by } f^{ext}} + [\underbrace{rN_j}_{\text{torque by } f_{(1,2)}^C} - \underbrace{r(2K\theta r + 2D\dot{\theta}r)}_{\text{torque by } f_{(1,2)}^P}]. \qquad (6)$$

Equation (6) governs the joint angle θ of a physical joint driven by the VAAM that is activated by the output N_j ($j \in \mathbb{Z}_{[1,18]}$) of the MNN. The joint angle θ and joint velocity $\dot{\theta}$ in Eq.(6) are not from sensory feedback but calculated from the fourth-order Runge-Kutta method. In principle, this bio-inspired compliant joint control approach (i.e., the VAAM) shares a connection to classical impedance control approaches [36] in terms of spring-damper based compliance. However, it is a biological modeling where muscle-like functions (e.g., variable compliant motions) are emulated by easily changing stiffness and damper parameters (i.e., K and D in Eq.(6)) [37].

A pair of agonist and antagonist mechanisms (e.g., the VAAM) gains advantage over a single antagonist or agonist mechanism in terms of the fast achievement of stability [37, 38]. This is because the VAAM can push and pull the joint at the same time generating inverse torques to oppose each other. Furthermore, some simulations have shown that a pair of agonist and antagonist muscles acting collaboratively produces more power than the sum of each muscle working independently [39].

3. The implementation of neuromechanical control

The outputs $O_{1-18} \in [-1, 1]$ of the neuromechanical controller are linearly scaled and transmitted to control the positions of the standard servo motors driving the 18 joints of the hexapod robot (see Fig. 6). For joint control, different control strategies are applied to swing and stance phases.

3.1. Swing phase

When a leg is in a swing phase (i.e., $f_i^{ext} = 0$, $i \in \mathbb{Z}_{[1,6]}$), the outputs $O_{(i,i+6,i+12)}$ for the TC, CTr and FTi joints receive the outputs of the motor neurons $N_{(i,i+6,i+12)}$ as their inputs. They satisfy:

$$[O_i, O_{i+6}, O_{i+12}]^T = [0.4N_i, 0.15N_{i+6}, -0.02N_{i+12}]^T - [0.05, -0.86, 0.43]^T, i \in \mathbb{Z}_{[1,6]}. \qquad (7)$$

The details of Eq.(7) can be seen in Appendix A.1 (i.e., see Eqs.(A.1), (A.2), and (A.3)).
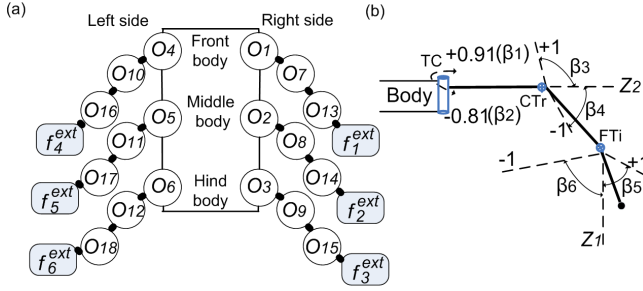
Figure 6: The outputs O_{1-18} of the neuromechanical controller. (a) O_{1-18} control 18 joints of the hexapod robot when receiving analog signals f^{ext}_{1-6}, which are detected by the force sensors at the legs. (b) Relationship between the joint outputs O_{1-18} and the joint angles θ_{1-18}. The angle ranges of the TC, CTr and FTi joints are as follows: $[\beta_1, \beta_2] = [0.32, -0.37](rad)$, $[\beta_3, \beta_4] = [-1.745, 0.785](rad)$, $[\beta_5, \beta_6] = [0.96, -1.222](rad)$.

3.2. Stance phase

According to the three-jointed legs of the hexapod robot, the TC joint of the leg allowing only horizontal motion is not affected by the PEs of the VAAM since there is only detection of vertical foot force at the end effector of the leg. As a consequence, the TC joint is driven by the CEs of the VAAM. In contrast, the CTr and FTi joints of the leg allowing vertical motion can be influenced by vertical foot force. The force therefore activates the PEs to generate variable compliant joint motions. To investigate proper compliant setups for the CTr and FTi joints, we test four possible control setups in a physical simulator (i.e., lpzrobots simulator [40]). A constraint for the setups is that each of them should contain at least the PEs for compliant generation. The simulation results show that setup 2 which is the combination of regular compliance at the CTr joint and sole compliance at the FTi joint is the best compared to other combinations (see Fig.7 (a)). This combination allows the hexapod robot to achieve better coordinated movement and stable locomotion with very low body oscillation (see Fig.7 (b)).
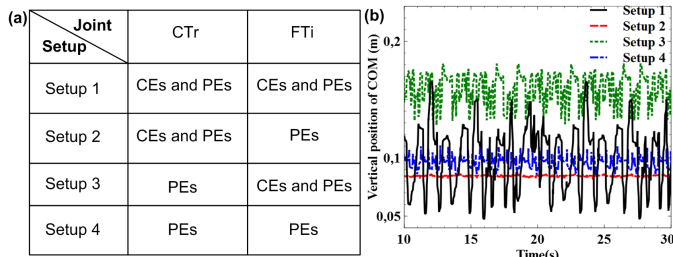

Figure 7: Four control setups for the CTr and FTi joints tested in a physical simulator. (a) Four control setups. (b) Vertical position of the hexapod robot. The vertical position shows that the hexapod robot walks stably (lower body oscillation) when the FTi joints are controlled by only the PEs of the VAAM, and the CTr joints are controlled by the CEs and PEs of the VAAM (i.e., setup 2).

Therefore, the control strategy of each three-jointed leg of the hexapod robot is as follows: each TC joint (i.e., proximal joint) is purely controlled by the CEs of the VAAM leading to pure actuation or no compliance, each CTr joint (i.e., intermediate joint) is governed by the CEs and PEs of the VAAM (combi-

nation of actuation and compliance resulting in regular compliance), and each FTi joint (i.e., distal joint) is driven by the PEs of the VAAM resulting in pure compliance (see Fig. 8). This control strategy also complies with the findings revealed by a biological study on three-jointed leg locomotion [41, 42]. The biological study shows that the proximal joints of animal legs mainly act as actuation while their distal joints serve as compliance and their intermediate joints show the combination.
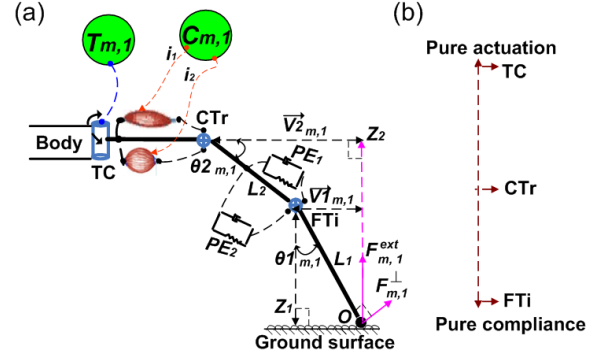

Figure 8: Neuromechanical control for each three-jointed leg. (a) The TC joint is controlled by the output of the TC motor neuron while the CTr joint is driven by the VAAM activated by the output of the CTr motor neuron. All outputs of the motor neurons come from the modular neural network (MNN). Besides, the FTi joint is driven by a pair of parallel elements (i.e., PE_1 and PE_2) of the VAAM. In this implementation, the TC joint has pure actuation while the CTr joint combines actuation and compliance and the FTi joint has only pure compliance. (b) The three-jointed leg control refers to the findings revealed by a biological study on three-jointed leg locomotion [41, 42].

The outputs O_{1-18} of the proposed neuromechanical controller are calculated as follows:

3.2.1. TC joints

All TC joints are purely controlled by $CE_{(1,2)}$ of the VAAM. The matrix of the outputs of the TC motor neurons is $T_{6\times1} = [N_1, N_2, \ldots, N_6]^T$. O_j are given by ($j \in \mathbb{Z}_{[1,6]}$):

$$O_j = 0.4T_{j,1} - 0.05. \qquad (8)$$

The details of Eq.(8) can be seen in Appendix A.2.1 (i.e., see Eq.(A.4)).

3.2.2. CTr joints

Each CTr joint is driven by $PE_{(1,2)}$ and $CE_{(1,2)}$ of the VAAM. The matrix $\theta2_{6\times1}$ of the CTr angles is the sum of the Hadamard products (see Eqs.(17-18) of our previous work [9]):

$$
\begin{aligned}
I\ddot{\theta2}_{6\times1} = & \; F^{ext}_{6\times1} \circ (L_2 \cos(\theta2_{6\times1}) + \vec{V1}_{6\times1}) \\
& + [rC_{6\times1} - \\
& 2r^2(K2_{6\times1} \circ \theta2_{6\times1} + D2_{6\times1} \circ \dot{\theta2}_{6\times1})].
\end{aligned}
\qquad (9)
$$

The angles $\theta2_{m,1}$ ($m \in \mathbb{Z}_{[1,6]}$, see $\theta2_{6\times1}$ in Eq.(9)) of the CTr joints are linearly transformed into their outputs O_j (see Fig. 6). O_j are given by ($j \in \mathbb{Z}_{[7,12]}$):

$$O_j = -0.8\theta2_{m,1} - 0.38, m = j - 6. \qquad (10)$$

The details of Eq.(10) can be seen in Appendix A.2.2 (i.e., see Eq.(A.5)).

3.2.3. FTi joints

Each FTi joint is only driven by $PE_{(1,2)}$ of the VAAM (see Fig. 8 (a)). The FTi angle matrix $\theta 1_{6\times 1}$ is the sum of the Hadamard products (see Eqs.(13-15) of our previous work [9]):

$$
\begin{aligned}
I\ddot{\theta}1_{6\times 1} = \ & F^{ext}_{6\times 1} \circ \sin(\theta 1_{6\times 1})L_1 \\
& - r(2rK1_{6\times 1} \circ \theta 1_{6\times 1} + 2rD1_{6\times 1} \circ \dot{\theta}1_{6\times 1}). \quad (11)
\end{aligned}
$$

The angles $\theta 1_{m,1}$ ($m \in \mathbb{Z}_{[1,6]}$, see $\theta 1_{6\times 1}$ in Eq.(11)) of the FTi joints can be linearly transformed into their outputs O_j (see Fig. 6). O_j are given by ($j \in \mathbb{Z}_{[13,18]}$):

$$
O_j = 0.92\theta 1_{m,1} + 0.12, m = j - 12. \quad (12)
$$

The details of Eq.(12) can be seen in Appendix A.2.3 (i.e., see Eq.(A.6)).

4. Experimental Results

The proposed neuromechanical controller can produce variable compliant motions, thereby leading to adaptive and energy efficient locomotion over different surfaces. The surfaces tested here include fine gravel (diameter φ = 5-8 mm), coarse gravel (φ = 16-25 mm), very coarse gravel (φ = 40-60 mm), floor, snow and sponge surfaces. The variable compliant motions are implemented by changing the stiffness coefficients of the FTi and CTr joints (i.e., $K1_{6\times 1}$ in Eq.(11) and $K2_{6\times 1}$ in Eq.(9)).

4.1. Setups of $K1_{6\times 1}$ and $K2_{6\times 1}$

We tested 2601 setups of $K1_{6\times 1}$ and $K2_{6\times 1}$ for the robot in the LpzRobot simulator [40]. By using these setups of $K1_{6\times 1}$ and $K2_{6\times 1}$, the forward displacements X of the robot are used to measure the performance of robot walking (see X in Fig. 9). With each setup, the running time of robot walking is 30s. One can see that the robot performs proper walking behavior on a flat surface when $K(1,2)_{6\times 1}$ are set within the range surrounded by black dash lines shown in Fig. 9. The result also certifies the bigdog-inspired control strategies [41, 42] (see Fig. 8). That is, the distal joints (e.g., FTi joints) should act more compliantly than the intermediate joints (e.g., CTr joints). Therefore, stiffness coefficients $K(1,2)_{m,1}$ should be set as: $K1_{m,1} < K2_{m,1}$ (e.g., $2 \times K1_{m,1} = K2_{m,1}$). Four setups of $K(1,2)_{m,1}$ are chosen for testing on our real hexapod robot ($m \in \mathbb{Z}_{[1,6]}$, see $S(1-4)$ in Fig. 9):

$S$1: $K1_{m,1} = 2$, $K2_{m,1} = 4$;
$S$2: $K1_{m,1} = 3$, $K2_{m,1} = 6$;
$S$3: $K1_{m,1} = 4$, $K2_{m,1} = 8$;
$S$4: $K1_{m,1} = 4.5$, $K2_{m,1} = 9$.

Note that all damper coefficients $D(1,2)_{m,1}$ are set to 1.0.

4.2. Real hexapedal robot walking on different surfaces

We tested the four setups (i.e., $S(1-4)$) of $K(1,2)_{6\times 1}$ on our real hexapod robot walking on fine gravel (diameter φ = 5-8 mm), coarse gravel (φ = 16-25 mm), very coarse gravel (φ = 40-60 mm), floor, snow (thickness 8cm), and sponge (stiffness 0.523 kN/m) surfaces. The hexapod robot had a difficulty to
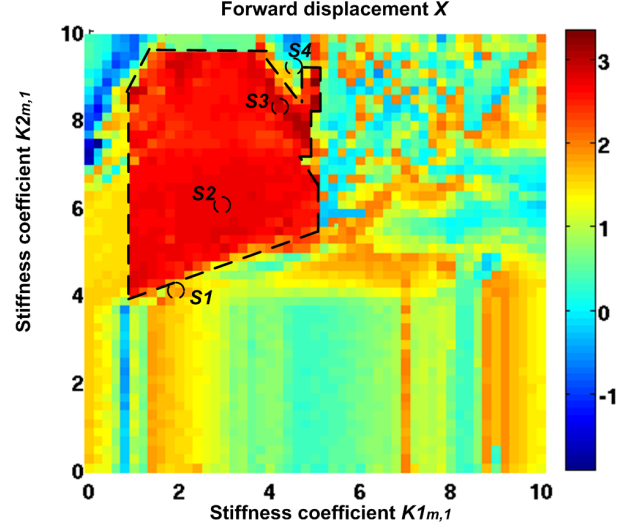

Figure 9: Forward displacements X (unit: m)according to the changes of the stiffness coefficients $K1_{m,1}$ and $K2_{m,1}$. Four sets (i.e., $S(1-4)$) of the stiffness coefficients $K(1,2)_{6\times 1}$ are used to test on our physical robot for walking over different surfaces.

walk on all these uneven surfaces when the lower stiffness setup (i.e., $S$1) was used. This is because with this setup the legs of the hexapod robot shallowly penetrate into the surfaces, thereby gaining less foot contact force (see $S$1 in Fig. 10). When the higher stiffness setup (i.e., $S$4) was used, the legs penetrate into the surfaces more deeply. However, this sometimes causes unstable locomotion which can be observed from dropping of the foot contact force (see A1 and A2 of $S$4 in Fig. 10). Therefore, with the steup $S$4 the robot also had a difficulty to overcome all these surfaces. Note that "high stiffness" (i.e., high impedance [43, 44]) here means that a joint greatly resists the influence of external forces; thereby low compliance. In contrast, "low stiffness" (i.e., low impedance [44, 45]) here means that a joint allows external forces to influence its movement easily; thereby high compliance.

Quantitatively, the inverse of compliance is stiffness, typically quantified by the ratio of the greatest magnitude of a sinusoidally varying force to the greatest magnitude of a displacement [46]. According to this, the stiffness Y_{j+6} and Y_{j+12} ($j = 1, 2, \ldots, 5, 6$) of the CTr and FTi joints is calculated as:

$$
\begin{aligned}
Y_{j+6} &= \left| \frac{Max(F^{ext}_{j,1})}{Min(O_{j+6}) - Ini(O_{j+6})} \right| = \left| \frac{Max(F^{ext}_{j,1})}{Min(O_{j+6})} \right|, \\
Y_{j+12} &= \left| \frac{Max(F^{ext}_{j,1})}{Min(O_{j+12}) - Ini(O_{j+12})} \right| = \left| \frac{Max(F^{ext}_{j,1})}{Min(O_{j+12})} \right|, \quad (13)
\end{aligned}
$$

where $Max(F^{ext}_{j,1})$ is the maximum value of an analog signal of the foot force $F^{ext}_{j,1}$ (e.g., see $F^{ext}_{1,1}$ in Fig. 11 (c)). $Min(O_{j+6})$ and $Min(O_{j+12})$ are the minimum values of the CTr and FTi joint outputs O_{7-18}, and $Ini(O_{j+6})$ and $Ini(O_{j+12})$ are their initial values, i.e., $Ini(O_{j+6}) = Ini(O_{j+12}) = 0$. The examples of the joint stiffness $Y7$ and $Y13$ are shown in Figs.11 and 12 when high and low stiffness setups were applied for walking on fine gravel and sponge.
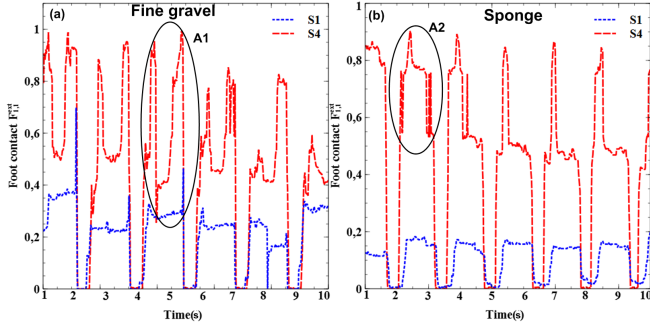
Figure 10: Analog signals of foot force with stiffness setups $S1$ and $S4$. The signals were sensed when the hexapod robot walked on final gravel and sponge surfaces.

In contrast to the setups $S1$ and $S4$, the setups $S2$ and $S3$ allow the hexapod robot to walk well on all these uneven surfaces. However, they lead to different energy efficiencies of walking on the different surfaces. Its energy-efficiency is here measured by the specific resistance ε [6, 7] as:

$$\varepsilon = \frac{P}{mgv}, \tag{14}$$

where P is power consumption. mg is the weight of the hexapod robot, i.e., $mg = 52.974$ N. v is its forward speed. For each stiffness setup (i.e.,$S2$ or $S3$), we ran the hexapod robot at each surface ten times. For each run, the power consumption P and average speed v_{avg} were obtained. The average specific resistances ε_{avg} with their standard deviations are shown in TABLE I. Low ε_{avg} corresponds to more energy efficient walking.

TABLE I
EXPERIMENTAL STATISTICS OF
AVERAGE SPECIFIC RESISTANCES WITH STANDARD DEVIATIONS

Setup \ Surface	Fine gravel	Coarse gravel	Very coarse gravel	Floor	Snow	Sponge
$S3$	9.1 ± 0.4	18.1 ± 0.7	25.0 ± 0.6	16.9 ± 0.7	18.8 ± 0.5	21.8 ± 0.9
$S2$	22.7 ± 0.5	20.7 ± 1.1	23.6 ± 0.5	14.0 ± 0.4	22.3 ± 0.8	19.7 ± 0.8

One can see that the high stiffness setup $S3$ allows more energy efficient locomotion (see TABLE I) on loose surfaces (i.e., fine and coarse gravels, snow). This is because $S3$ enables the hexapod robot to obtain more foot contact force (e.g., see Fig. 11 (c)) on these surfaces owing to stiffer CTr and FTi joints (e.g., see Figs. 11 (d) and (e)). Whereas the low stiffness setup $S2$ results in more force (e.g., see Fig. 12 (c)) on flat (e.g., floor), very coarse (e.g., gravels), and elastic (e.g., sponge) surfaces. Therefore, $S2$ leads to more energy efficient locomotion on these surfaces due to softer legs (e.g., see joint stiffness in Figs. 12 (d) and (e)). Interestingly, this experimental result shows that soft legs allow the hexapod robot to achieve more energy-efficient locomotion on a soft elastic surface (e.g., sponge). The finding complies with a finding of physiological experiments on cockroach locomotion [47, 12]. Owing to energy efficiency, cockroaches also use their soft legs on soft elastic surfaces.

In addition, the neuromechanical controller leads to more energy-efficient AMOS walking over three surfaces, compared
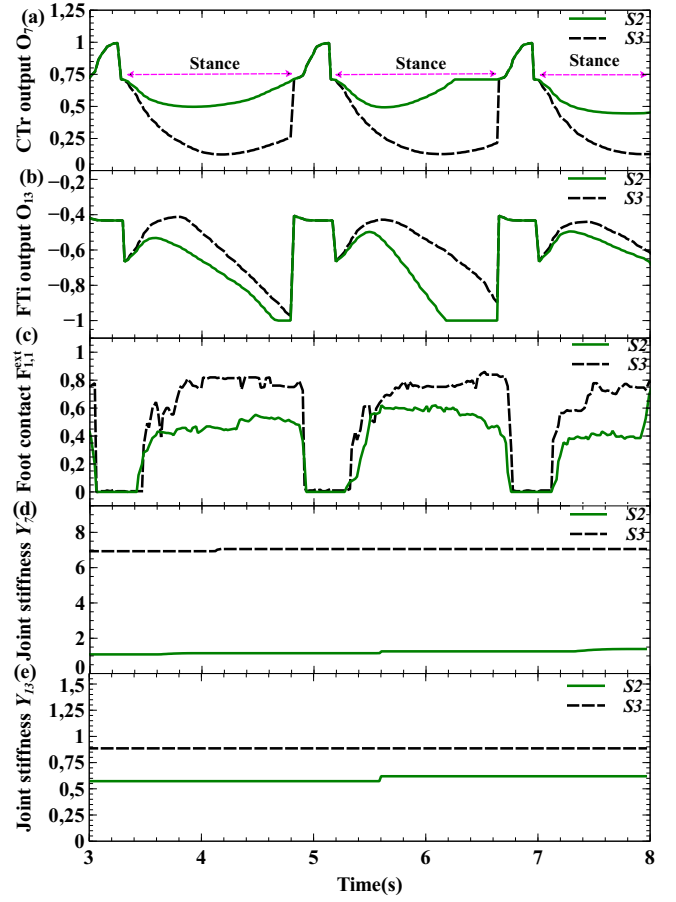

Figure 11: Joint outputs, foot force signals, and joint stiffness that resulted from two stiffness setups $S(2, 3)$ during walking on fine gravel. (a) CTr joint outputs O_7. (b) FTi joint outputs O_{13}. (c) Analog signals of forces $F_{1,1}^{ext}$. The setup $S3$ enables the hexapod robot to obtain more foot contact force during stance phases than the setup $S2$. (d) CTr joint stiffness Y_7. (e) FTi joint stiffness Y_{13}. The joint stiffness Y_7 and Y_{13} are calculated by Eq.(13). The setup $S3$ makes the legs stiffer than the setup $S2$.

to an adaptive neural controller [11] (see TABLE II). For example, the specific resistance of walking on the fine gravel surface using the adaptive neural controller is 55.5 while the specific resistance can be reduced to 9.1 when the neuromechanical controller with the high stiffness setup (i.e., $S3$) was employed. This is because the neuromechanical controller stiffens and enables AMOS legs to penetrate deeply into the surface; thereby gaining more foot contact force for propelling the body forwards. Whereas the adaptive neural controller cannot drive the legs to penetrate deeply into the surfaces due to the lack of stiffening them. Note that both controllers use the same modular neural network (see Fig. 3) and control input for gait generation (i.e., S = 0.04, see Fig. 4). They were also tested on the same hexapod robot (i.e., AMOS).

4.3. Surface classifications

Among the four stiffness setups, $S3$ is better for the hexapod robot to achieve energy efficient locomotion over fine and coarse gravels. With $S3$, we ran the hexapod robot from fine gravel to coarse gravel. The CTr and FTi joint signals (i.e., O_7
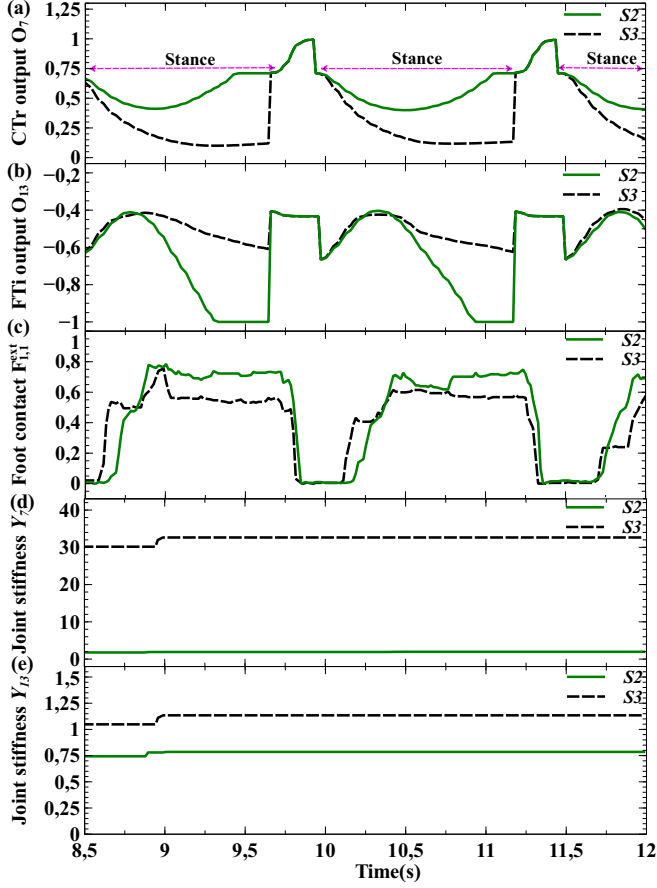
Figure 12: Joint outputs, foot force signals, and joint stiffness that resulted from two stiffness setups $S(2,3)$ during walking on sponge. (a) CTr joint outputs O_7. (b) FTi joint outputs O_{13}. (c) Analog signals of forces $F_{1,1}^{ext}$. The setup $S2$ enables the hexapod robot to obtain more foot contact force during stance phases than the setup $S3$. (d) CTr joint stiffness Y_7. (e) FTi joint stiffness Y_{13}. The joint stiffness Y_7 and Y_{13} are calculated by Eq.(13). The setup $S3$ makes the legs stiffer than the setup $S2$.

TABLE II
COMPARISONS OF AVERAGE SPECIFIC RESISTANCES

surface Controller	Fine gravel	Coarse gravel	Floor
Neuromechanical controller	9.1 ± 0.4	18.1 ± 0.7	14.0 ± 0.4
Adaptive neural controller	55.5 ± 6.1	24.5 ± 1.1	21.9 ± 1.2

and O_{13}) of its right front leg are shown in Fig.13. One can see that the hexapod robot can autonomously adapt its CTr and FTi joint motions during walking on the surfaces. Other different FTi joint signals can be seen in Fig. 14 when the hexapod robot walked on sponge and snow. Therefore, the FTi joint signals can be used to classify the surfaces. One can see that it is hard for a legged robot to classify floor, snow and sponge surfaces by visual perception due to their non-distinguishable features (see Fig. 15).

We ran the hexapod robot on six different surfaces, respectively. Six FTi outputs (i.e., O_{13}) of the right front leg were obtained as order datum streams $FT_j(t)$ and used as the inputs of the cumulative moving averages (CMA). The CMA outputs
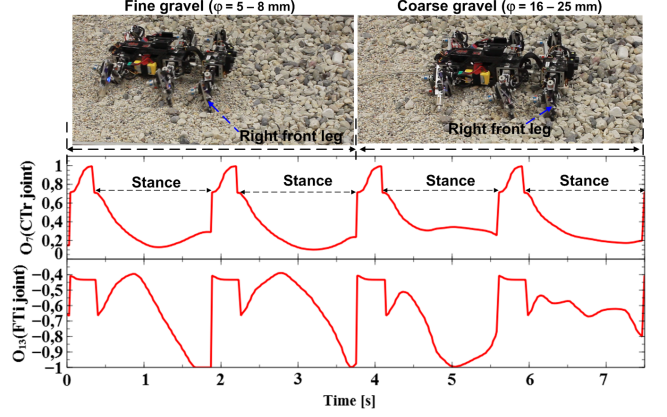

Figure 13: CTr and FTi joint signals(i.e., O_7 and O_{13}) of the right front leg. O_7 and O_{13} show adaptable walking of the hexapod robot when it walked from fine gravel (diameter φ = 5-8 mm) to coarse gravel (φ = 16-25 mm).
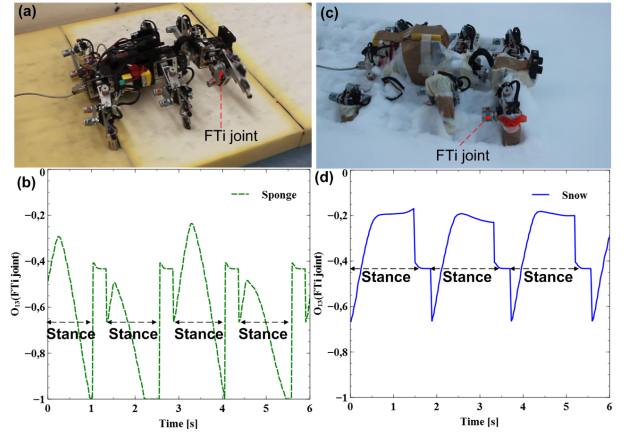

Figure 14: The hexapod robot walked on sponge and snow surfaces. (a) Snapshot of walking on sponge. (b) FTi joint signal O_{13} of walking on sponge. (c) Snapshot of walking on snow (d) FTi joint signal O_{13} of walking on snow.

$CA_j(t)$ are given by:

$$CA_j(t) = CA_j(t - \Delta t) + \frac{FT_j(t) - CA_j(t - \Delta t)}{\frac{t}{\Delta t} + 1}, \Delta t \le t \le 14,$$

(15)

where j denotes the type of the surface (i.e., $j \in \mathbb{Z}_{[1,6]}$), i.e., $j = 1 - 6$ denote fine gravel, coarse gravel, very coarse gravel, floor, snow and sponge surfaces. t is a discrete time domain (i.e., 0s − 14s) at the interval $\Delta t \approx 0.019$s. The initial value $CA_j(0)$ is set to $FT_j(0)$.

The CMA outputs $CA_j(t)$ shown in Fig.(16) are used as sample signals for the surface classifications. Then we ran the hexapod robot on nine sets of the six surfaces. The total number of the runs is 54. For each run, the CMA output $CA(t)$ is calculated by Eq.(15). The deviations DEV_j between $CA(t)$ and $CA_j(t)$ are given by:

$$DEV_j = \sum_{t=0}^{14}(|CA(t) - CA_j(t)|), j = 1, 2, \ldots, 5, 6,$$

$$SC = min(DEV_j), \text{when h = j.} \quad (16)$$

SC is the minimal value of the deviations DEV_j. h is the result

Figure 15: Six different surfaces used in the experiments.

of the classification for the run ($h \in \mathbb{Z}_{[1,6]}$). h is set to $1-6$ denoting fine gravel, coarse gravel, very coarse gravel, floor, snow, and sponge surfaces, respectively. For example, if SC is DEV_2 (i.e., $h = 2$), the result of the surface classification is coarse gravel.
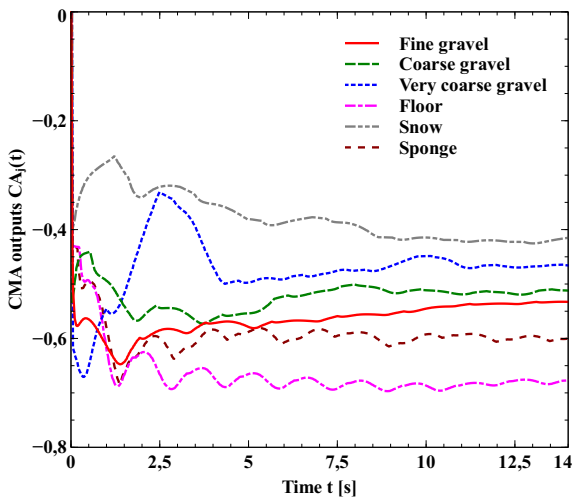

Figure 16: Cumulative moving average (CMA) outputs $CA_j(t)$.

The experimental statistics (i.e., the numbers of correct and wrong classifications) of the surface classifications is shown in TABLE III. One can see that eight of nine runs are classified correctly for fine gravel and coarse gravel surfaces. Thus, the success rates of classifying fine gravel and coarse gravel surfaces are 89%. The success rate (SR) is used to evaluate the performance of surface classifications, which is the ratio of the number of correctly classifying a given surface and the total number of classifications on this surface. SR = 100% is found for the classifications of very coarse gravel, floor, snow and sponge surfaces (see TABLE III). We emphasize that the ability of well terrain classification presented here is due to the exploitation of compliance signals generated by the VAAMs. Here, the signals are determined by the motions of the FTi joints. From this point of view, the VAAMs are one of key components enabling the hexapod robot to well classify some types of surfaces where the robot moves. Note that the key components include force sensing, the VAAMs, and the cumulative moving average algorithm.

TABLE III
EXPERIMENTAL STATISTICS OF THE SURFACE CLASSIFICATIONS

Sample / Classified as	Fine gravel	Coarse gravel	Very coarse gravel	Floor	Snow	Sponge	SR
Fine gravel	8	1	0	0	0	0	89%
Coarse gravel	1	8	0	0	0	0	89%
Very coarse gravel	0	0	9	0	0	0	100%
Floor	0	0	0	9	0	0	100%
Snow	0	0	0	0	9	0	100%
Sponge	0	0	0	0	0	9	100%

5. Discussion

Here, we briefly discuss some aspects of neuromechanical control for legged locomotion, since most of the relevant discussions have been provided in above sections. The motivations and benefits of neuromechanical control are in detailed described in [48, 1, 8, 2] compared to pure neural control or mechanical control (e.g., compliance control). Many neuromechanical controllers have been developed for different types of locomotion, e.g., salamander-like trotting [3, 49], lamprey-like swimming [4, 50] and insect-like walking [5, 51]. However, rather than physical robot implementations, most of them are only presented by computer simulations owing to their complexities. For instance, a neuromechanical model of insect locomotion uses 264 ordinary differential equations (ODEs) for describing its central pattern generator, muscles actuating jointed legs, and joint torque feedback to motoneurons [52]. By using phase reduction and average theory, the model is reduced to 24 one-dimensional phase oscillators activating agonist-antagonist muscle pairs shown in later works [5, 53]. However for the muscles, there are up to 26 parameters to be tuned in the model, which is impractical for applying it to physical legged robots. Different from this, agonist-antagonist muscles can be physically implemented by artificial muscles (e.g., fluidic muscles) [54, 55]. For instance, some insect-like robots use McKibben fluidic muscles as their actuators, e.g., AirBug (weight 27.2 kg) [56] and Robot V (Ajax) (weight 15.1 kg) [57]. But these artificial muscles make the mechanical structures of legged robots more complex and bulky, therefore rarely presenting their use in small legged robots (weight less than 8 kg) [21]. Whereas the virtual agonist-antagonist mechanism introduced here is a muscle model with only two tunable parameters. It can be easily applied to generate variable compliant leg motions of small legged robots. These applications do not require force/torque sensing at each joint or physical compliant components (e.g., springs or artificial muscles). The proposed neuromechanical controller is based on biological findings [13, 47, 12] and can improve the energy efficiency of a hexapod robot. The specific resistances of the robot during walking on different surfaces are between 9.1 and 25.0 (i.e., ε = 9.1-25.0) (see TABLE I). On surfaces, like fine gravel, coarse gravel, and floor, the specific resistances are less than the ones obtained from walking driven by the adaptive neural controller (see TABLE II).

As a comparison, the specific resistance of the RHex robot (i.e., a hexapod robot) is between 2 and 14 [7] when it ran

on different surfaces (i.e., gravels). Considering that the RHex robot has only one degree of freedom (DOF) for each leg (totally six motors), our robot consisting of three DOFs for each leg (totally 18 motors) consumes more energy. However thanks to the three DOFs for each leg, our robot can reproduce insect-like leg movements, and its legs can be extended for climbing [58] as well as allow for omnidirectional walking including sideways walking [34].

Taken together our main contributions here which is an extension of our previous work [9] include: 1) the experimental part dealing with in more details of parameter setups (stiffness coefficients $K(1, 2)$, see section 4.1) which can be applied to other legged robots, 2) the new walking experiments on six challenging surfaces (see section 4.2), and 3) the exploitation of compliance signals generated by the VAAMs for surface classifications (see section 4.3).

6. CONCLUSIONS

We developed a neuromechanical controller that allows for variable compliant leg motions of a hexapod robot, thereby leading to its adaptable and energy-efficient walking on six challenging surfaces. The controller consists of a modular neural network (MNN) and virtual agonist-antagonist mechanisms (VAAMs, i.e., a muscle model). The main features of the neuromechanical controller are as follows: (I) It allows the hexapod robot to easily achieve variable leg compliance by only changing the stiffness parameters of the VAAMs. The implementation does not require any passive mechanisms or torque and position feedback; (II) The VAAMs also enable the hexapod robot to classify six different surfaces with high success rates; (III) It presents a control strategy on the three-jointed leg of the hexapod robot which also agrees to the principles found in the biological study on three-jointed leg locomotion [41, 42]. In future work, the surface classification will be used for the hexapod robot to autonomously change its leg compliance with respect to a surface. Moreover, we will also apply a learning mechanism for the adaptation of muscle parameters on different surfaces.

7. Acknowledgment

Appendix A. Neuromechanical control of the legs

Appendix A.1. Swing phase

When a leg is in a swing phase (i.e., $f_i^{ext} = 0$, $i \in \mathbb{Z}_{[1,6]}$, see Fig. 6 (a)), outputs $O_{(i,i+6,i+12)}$ for its TC, CTr and FTi joints receive the outputs of the motor neurons $N_{(i,i+6,i+12)}$ as their inputs.

Appendix A.1.1. TC joints

The TC neuron outputs $N_{1-6} \in [-0.81, 0.91]$ are scaled into the TC outputs $O_{1-6} \in [-0.37, 0.32]$:

$$
\begin{aligned}
O_{1-6} &= \frac{N_{1-6} - (-0.81)}{0.91 - (-0.81)}(0.32 - (-0.37)) - 0.37 \\
&\approx 0.4 N_{1-6} - 0.05.
\end{aligned}
\tag{A.1}
$$

Appendix A.1.2. CTr joints

The CTr neuron outputs $N_{7-12} \in [-1, 0, 1.0]$ are scaled into the CTr outputs $O_{7-12} \in [0.71, 1.0]$:

$$
\begin{aligned}
O_{7-12} &= \frac{N_{7-12} - (-1.0)}{1.0 - (-1.0)}(1.0 - 0.71) + 0.71 \\
&\approx 0.15 N_{7-12} + 0.86.
\end{aligned}
\tag{A.2}
$$

Appendix A.1.3. FTi joints

The FTi neuron outputs $N_{13-18} \in [-0.9, 1.0]$ are scaled into the FTi outputs $O_{13-18} \in [-0.41, -0.45]$:

$$
\begin{aligned}
O_{13-18} &= \frac{N_{13-18} - (-0.9)}{1.0 - (-0.9)}((-0.45) - (-0.41)) - 0.41 \\
&\approx -0.02 N_{13-18} - 0.43.
\end{aligned}
\tag{A.3}
$$

Appendix A.2. Stance phase

Appendix A.2.1. TC joints

All TC joints are purely controlled by $CE_{(1,2)}$ of the VAAM. $CE_{(1,2)}$ are activated by the outputs N_{1-6} of the modular neural network. The TC neuron outputs $T_{j,1} \in [-0.81, 0.91]$ are scaled into the TC outputs $O_j \in [-0.37, 0.32]$ (see Fig. 8 (a), $j \in \mathbb{Z}_{[1,6]}$):

$$
\begin{aligned}
O_j &= \frac{T_{j,1} - (-0.81)}{0.91 - (-0.81)}(0.32 - (-0.37)) - 0.37 \\
&\approx 0.4 T_{j,1} - 0.05.
\end{aligned}
\tag{A.4}
$$

Appendix A.2.2. CTr joints

Each CTr joint is driven by $PE_{(1,2)}$ and $CE_{(1,2)}$ of the VAAM. $CE_{(1,2)}$ are activated by one of the outputs N_{7-12} of the modular neural network (see Fig. 8 (a)). The angles $\theta 2_{m,1}$ ($m \in \mathbb{Z}_{[1,6]}$) of the CTr joints are linearly transformed into their outputs O_j (see Fig. 6). O_j are given by ($j \in \mathbb{Z}_{[7,12]}$):

$$
\begin{aligned}
O_j &= \frac{\theta 2_{j-6,1} - 0.785}{-1.745 - 0.785}(1 - (-1)) - 1 \\
&\approx -0.8 \theta 2_{j-6,1} - 0.38
\end{aligned}
\tag{A.5}
$$

Appendix A.2.3. FTi joints

Each FTi joint is only driven by $PE_{(1,2)}$ of the VAAM (see Fig. 8 (a)). The angles $\theta 1_{m,1}$ ($m \in \mathbb{Z}_{[1,6]}$) of the FTi joints can be linearly transformed into their outputs O_j (see Fig. 6). O_j are given by ($j \in \mathbb{Z}_{[13,18]}$):

$$
\begin{aligned}
O_j &= \frac{\theta 1_{j-12,1} - (-1.22)}{0.96 - (-1.22)}(1 - (-1)) - 1 \\
&\approx 0.92\theta 1_{j-12,1} + 0.12.
\end{aligned} \tag{A.6}
$$

Appendix B. Notations

- $F^{ext}_{6\times1}$ is the matrix of the forces, i.e., $F^{ext}_{6\times1} = [f^{ext}_1, f^{ext}_2, \ldots, f^{ext}_6]^T$;

- $F^{\perp}_{6\times1}$ is the Hadamard product of $F^{ext}_{6\times1}$ and $\sin(\theta 1_{6\times1})$;

- L_1 is the length of the link between the FTi joint and the end effector of the leg, e.g., $L_1 = 0.115$ m;

- I is the inertia of the FTi and CTr joints, i.e., $I = 0.5\times10^{-3}$;

- $\ddot{\theta} 1_{6\times1}$ and $\dot{\theta} 1_{6\times1}$ are the acceleration and velocity matrices of $\theta 1_{6\times1}$. r is set to 0.1;

- $K(1,2)_{6\times1}$ and $D(1,2)_{6\times1}$ are matrices of the stiffness and damper coefficients of $PE_{(1,2)}$, which control the compliance of the FTi and CTr joints.

- L_2 is the length of links between the CTr and FTi joints, i.e., $L_2 = 0.075$ m;

- $\vec{V} 1_{6\times1}$ and $\vec{V} 2_{6\times1}$ are matrices of the displacement vectors of the CTr and FTi joints relating to the forces f^{ext}_{1-6}.

- $\ddot{\theta} 2_{6\times1}$ and $\dot{\theta} 2_{6\times1}$ are the acceleration and velocity matrices of $\theta 2_{6\times1}$.

- $C_{6\times1}$ is the matrix of the CTr neuron outputs of the MNN, i.e., $C_{6\times1} = [N_7, N_8, \ldots, N_{12}]^T$.

[1] K. Nishikawa, A. A. Biewener, P. Aerts, A. N. Ahn, H. J. Chiel, M. A. Daley, T. L. Daniel, R. J. Full, M. E. Hale, T. L. Hedrick, A. K. Lappin, T. R. Nichols, R. D. Quinn, R. A. Satterlie, B. Szymik, Neuromechanics: an integrative approach for understanding motor control, Integrative and Comparative Biology 47 (1) (2007) 16–54.

[2] L. A. Miller, D. I. Goldman, T. L. Hedrick, E. D. Tytell, Z. J. Wang, J. Yen, S. Alben, Using computational and mechanical models to study animal locomotion, Integrative and Comparative Biology 52 (5) (2012) 553–575.

[3] N. Harischandra, J.-M. Cabelguen, Ö. Ekeberg, A 3d musculo-mechanical model of the salamander for the study of different gaits and modes of locomotion, Frontiers in Neurorobotics 4 (112).

[4] E. D. Tytell, C.-Y. Hsu, T. L. Williams, A. H. Cohen, L. J. Fauci, Interactions between internal forces, body stiffness, and fluid environment in a neuromechanical model of lamprey swimming, Proceedings of the National Academy of Sciences.

[5] J. Proctor, R. P. Kukillaya, P. Holmes, A phase-reduced neuro-mechanical model for insect locomotion: feed-forward stability and proprioceptive feedback, Philosophical Transactions of the Royal Society A: Mathematical,Physical and Engineering Sciences 368 (1930) (2010) 5087–5104.

[6] P. Gregorio, M. Ahmadi, M. Buehler, Design, control, and energetics of an electrically actuated legged robot, Systems, Man, and Cybernetics, Part B: Cybernetics, IEEE Transactions on 27 (4) (1997) 626 –634.

[7] U. Saranli, M. Buehler, D. E. Koditschek, Rhex: A simple and highly mobile hexapod robot, The International Journal of Robotics Research 20 (7) (2001) 616–631.

[8] E. Tytell, P. Holmes, A. Cohen, Spikes alone do not behavior make: why neuroscience needs biomechanics, Current Opinion in Neurobiology 21 (5) (2011) 816 – 822, networks, circuits and computation.

[9] X. Xiong, F. Wörgötter, P. Manoonpong, A neuromechanical controller of a hexapod robot for walking on sponge, gravel and snow surfaces, in: Advances in Artificial Life. Proceedings of the 11th European Conference on Artificial Life ECAL 2013, 2013, pp. 989–996.

[10] P. Arena, L. Fortuna, M. Frasca, L. Patane, M. Pavone, Realization of a cnn-driven cockroach-inspired robot, in: Circuits and Systems, 2006. ISCAS 2006. Proceedings. 2006 IEEE International Symposium on, May, pp. 2649–2652.

[11] P. Manoonpong, U. Parlitz, F. Wörgötter, Neural control and adaptive neural forward models for insect-like, energy-efficient, and adaptable locomotion of walking machines, Frontiers in Neural Circuits 7 (12).

[12] A. J. Spence, Control strategies for legged locomotion: a comparative approach, in: 7th European Nonlinear Dynamics Conference (ENOC), Rome, Italy., 2011.

[13] S. Sponberg, R. J. Full, Neuromechanical response of musculo-skeletal structures in cockroaches during rapid running on rough terrain, Journal of Experimental Biology 211 (3) (2008) 433–446.

[14] T. E. Higham, A. A. Biewener, S. L. Delp, Mechanics, modulation and modelling: how muscles actuate and control movement, Philosophical Transactions of the Royal Society B: Biological Sciences 366 (1570) (2011) 1463–1465.

[15] D. F. B. Haeufle, S. Grimmer, A. Seyfarth, The role of intrinsic muscle properties for stable hopping-stability is achieved by the force-velocity relation, Bioinspiration & Biomimetics 5 (1) (2010) 016004.

[16] S. Sponberg, A. J. Spence, C. H. Mullens, R. J. Full, A single muscle's multifunctional control potential of body dynamics for postural control and running, Philosophical Transactions of the Royal Society B: Biological Sciences 366 (1570) (2011) 1592–1605.

[17] S. Sponberg, T. Libby, C. H. Mullens, R. J. Full, Shifts in a single muscle's control potential of body dynamics are determined by mechanical feedback, Philosophical Transactions of the Royal Society B: Biological Sciences 366 (1570) (2011) 1606–1620.

[18] N. Kohut, A. Hoover, K. Ma, S. Baek, R. Fearing, Medic: A legged millirobot utilizing novel obstacle traversal, in: Robotics and Automation (ICRA), 2011 IEEE International Conference on, May, pp. 802–808.

[19] E. Garcia, P. de Santos, On the improvement of walking performance in natural environments by a compliant adaptive gait, Robotics, IEEE Transactions on 22 (6) (2006) 1240–1253.

[20] R. Ham, T. Sugar, B. Vanderborght, K. Hollander, D. Lefeber, Compliant actuator designs, Robotics Automation Magazine, IEEE 16 (3) (2009) 81–94.

[21] K. C. Galloway, Passive variable compliance for dynamic legged robots, Phd thesis, University of Pennsylvania (2010).

[22] X. Xiong, F. Wörgötter, P. Manoonpong, A simplified variable admittance controller based on a virtual agonist-antagonist mechanism for robot joint control, in: Proc. Intl Conf. on Climbing and Walking Robots CLAWAR 2013, Sydney, Australia, 2013, pp. 281–288.

[23] T. Birnschein, G. Natarajan, S. Bartsch, F. Cordes, D. Kühn, F. Kirchner, Terrain recognition and environment modeling in legged robots, in: Proceedings of the 11th European Regional Conference of the International Society for Terrain-Vehicle Systems, o.A., 2009.

[24] S. Bartsch, T. Birnschein, M. Rämmermann, J. Hilljegerdes, D. Kühn, F. Kirchner, Development of the six-legged walking and climbing robot spaceclimber, Journal of Field Robotics 29 (3) (2012) 506–532.

[25] A. Schmidt, K. Walas, The classification of the terrain by a hexapod robot, in: R. Burduk, K. Jackowski, M. Kurzynski, M. Wozniak, A. Zolnierek (Eds.), Proceedings of the 8th International Conference on Computer Recognition Systems CORES 2013, Vol. 226 of Advances in Intelligent Systems and Computing, Springer International Publishing, 2013, pp. 825–833.

[26] M. Hoepflinger, C. Remy, M. Hutter, L. Spinello, R. Siegwart, Haptic terrain classification for legged robots, in: Robotics and Automation (ICRA), 2010 IEEE International Conference on, May, pp. 2828–2833.

[27] F. Bermudez, R. Julian, D. Haldane, P. Abbeel, R. Fearing, Performance analysis and terrain classification for a legged robot over rough terrain,

11

in: Intelligent Robots and Systems (IROS), 2012 IEEE/RSJ International Conference on, 2012, pp. 513 –519.

[28] P. Giguere, G. Dudek, S. Saunderson, C. Prahacs, Environment identification for a running robot using inertial and actuator cues, in: Proceedings of Robotics: Science and Systems, Philadelphia, USA, 2006.

[29] P. Filitchkin, K. Byl, Feature-based terrain classification for littledog, in: Intelligent Robots and Systems (IROS), 2012 IEEE/RSJ International Conference on, Oct., pp. 1387–1392.

[30] S. Zenker, E. Aksoy, D. Goldschmidt, F. Wörgötter, P. Manoonpong, Visual terrain classification for selecting energy efficient gaits of a hexapod robot, in: Advanced Intelligent Mechatronics (AIM), 2013 IEEE/ASME International Conference on, 2013, pp. 577–584.

[31] H. Bay, A. Ess, T. Tuytelaars, L. V. Gool, Speeded-up robust features (surf), Computer Vision and Image Understanding 110 (3) (2008) 346 – 359, similarity Matching in Computer Vision and Multimedia.

[32] J. C. Jacob Shill, Emmanuel Collins, Tactile terrain classification technique for legged robots, Pensacola, Florida., Dynamic Walking Conference, 2012.

[33] D. A. McCrea, I. A. Rybak, Organization of mammalian locomotor rhythm and pattern generation, Brain Research Reviews 57 (1) (2008) 134 – 146.

[34] P. Manoonpong, F. Pasemann, F. Wörgötter, Sensor-driven neural control for omnidirectional locomotion and versatile reactive behaviors of walking machines, Robotics and Autonomous Systems 56 (3) (2008) 265 – 288.

[35] S. Heitmann, M. Breakspear, N. Ferns, Muscle co-contraction modulates damping and joint stability in a three-link bio mechanical limb, Frontiers in Neurorobotics 5 (5).

[36] N. Hogan, S. P. Buerger, Impedance and Interaction Control, Vol. Chapter 19 of Robotics and Automation Handbook, CRC Press, 2004.

[37] X. Xiong, F. Wörgötter, P. Manoonpong, Virtual agonist-antagonist mechanisms produce biological muscle-like functions: An application for robot joint control, Industrial Robot: An International Journal 41 (4) (2014) 340 – 346.

[38] R. Shadmehr, S. P. Wise, The Computational Neurobiology of Reaching and Pointing, MIT Press, 2005.

[39] W. A. Farahat, H. M. Herr, Optimal workloop energetics of muscle-actuated systems: An impedance matching view, PLoS Comput Biol 6 (6) (2010) e1000795.

[40] R. Der, G. Martius, The lpzrobots simulator, in: The Playful Machine, Vol. 15 of Cognitive Systems Monographs, Springer Berlin Heidelberg, 2012, pp. 293–308.

[41] D. V. Lee, M. P. McGuigan, E. H. Yoo, A. A. Biewener, Compliance, actuation, and work characteristics of the goat foreleg and hindleg during level, uphill, and downhill running, Journal of Applied Physiology 104 (1) (January 2008) 130–141.

[42] M. Raibert, Bigdog, the rough-terrain quadruped robot, in: M. J. Chung (Ed.), Proceedings of the 17th IFAC World Congress, 2008, Vol. 17.

[43] G. Pratt, Legged robots at mit: what's new since raibert?, Robotics Automation Magazine, IEEE 7 (3) (2000) 15–19.

[44] G. A. Pratt, Low impedance walking robots, Integrative and Comparative Biology 42 (1) (2002) 174–181.

[45] J. Pratt, B. Krupp, C. Morse, Series elastic actuators for high fidelity force control, Industrial Robot: An International Journal 29 (Iss: 3) (2002) 234 – 241.

[46] D. M. Dudek, R. J. Full, Passive mechanical properties of legs from running insects, The Journal of Experimental Biology 209 (8) (2006) 1502–1515.

[47] A. J. Spence, S. Revzen, J. Seipel, C. Mullens, R. J. Full, Insects running on elastic surfaces, The Journal of Experimental Biology 213 (11) (2010) 1907–1920.

[48] P. Holmes, R. Full, D. Koditschek, J. Guckenheimer, The dynamics of legged locomotion: Models, analyses, and challenges, SIAM Review 48 (2) (2006) 207–304.

[49] N. Harischandra, J. Knuesel, A. Kozlov, A. Bicanski, J.-M. Cabelguen, A. J. Ijspeert, Ö. Ekeberg, Sensory feedback plays a significant role in generating walking gait and in gait transition in salamanders: A simulation study, Frontiers in Neurorobotics 5 (3).

[50] T. McMillen, T. Williams, P. Holmes, Nonlinear muscles, passive viscoelasticity and body taper conspire to create neuromechanical phase lags in anguilliform swimmers, PLoS Comput Biol 4 (8) (2008) e1000157.

[51] S. Knops, T. I. Tóth, C. Guschlbauer, M. Gruhn, S. Daun-Gruhn, A neuromechanical model for the neuronal basis of curve walking in the stick insect, Journal of Neurophysiology 109 (3) (2013) 679–691.

[52] R. Kukillaya, J. Proctor, P. Holmes, Neuromechanical models for insect locomotion: Stability, maneuverability, and proprioceptive feedback, Chaos: An Interdisciplinary Journal of Nonlinear Science 19 (2).

[53] J. Proctor, P. Holmes, Reflexes and preflexes: on the role of sensory feedback on rhythmic patterns in insect locomotion, Biological Cybernetics 102 (6) (2010) 513–531.

[54] R. King, State of the art in robotics and robotic actuation, in: BiLBIQ: A Biologically Inspired Robot with Walking and Rolling Locomotion, Vol. 2 of Biosystems & Biorobotics, Springer Berlin Heidelberg, 2013, pp. 29–47.

[55] R. Dillmann, J. Albiez, B. Gaßmann, T. Kerscher, M. Zöllner, Biologically inspired walking machines: design, control and perception, Philosophical Transactions of the Royal Society A: Mathematical,Physical and Engineering Sciences 365 (1850) (2007) 133–151.

[56] R. Dillmann, J. Albiez, B. Gaßmann, T. Kerscher, Biologically motivated control of walking machines, in: Climbing and Walking Robots, Springer Berlin Heidelberg, 2005, pp. 55–69.

[57] D. Kingsley, R. Quinn, R. E. Ritzmann, A cockroach inspired robot with artificial muscles, in: Intelligent Robots and Systems, 2006 IEEE/RSJ International Conference on, 2006, pp. 1837–1842.

[58] D. Goldschmidt, F. Hesse, F. Wörgötter, P. Manoonpong, Biologically inspired reactive climbing behavior of hexapod robots, in: Intelligent Robots and Systems (IROS), 2012 IEEE/RSJ International Conference on, 2012, pp. 4632–4637.